Published in Marine Geology 250, issues 1-2, 128-141, 2008
which should be used for any reference to this work

Characterization of metalliferous sediment from a low temperature hydrothermal environment on the Eastern Flank of the East Pacific Rise.

S. Bodeï [a*], M. Buatier [a], M. Steinmann [a], T. Adatte [b], C.G. Wheat [c]

[a] Département Géosciences, EA2642, UFR Sciences et Technique, Université de Franche Comté, 16 Route de Gray, 2503 Besançon, France.
(sabine.bodei@univ-fcomte.fr;
martine.buatier@univ-fcomte.fr, marc.steinmann@univ-fcomte.fr)

[b] University of Neuchâtel, Institute of geology, Emile-Argand 11, CH-2007 Neuchâtel, Switzerland. (thierry.adatte@unine.ch)

[c] Global Undersea Research Unit, Univ. Of Alaska Fairbanks, P.O Box 757 220 Fairbanks, Alaska 99775, USA. (wheat@mbari.org)

Corresponding author. Tel: +33 (0)3 81 66 64 31; fax: +33 (0)3 81 66 65 58; e-mail: sabine.bodei@univ-fcomte.fr

Abstract

Metalliferous deposits are described from the eastern flank of the East Pacific Rise (EPR) offshore Costa Rica, close to a basaltic seamount called “Dorado high”. Based on heat-flow data and porewater profiles, the site is an area of active low temperature hydrothermal discharge. We focus on the mineralogical and chemical analyses from a 124 cm long gravity core (GC50), located on the north-western slope of the 100 m high Dorado high. In this core, the sediments consist of detrital clay minerals as well as authigenic minerals such as zeolites, apatites, and Fe/Mn-rich oxy-hydroxides. In contrast, the reference sediments from adjacent areas without hydrothermal activity are olive gray hemipelagic muds composed of volcanic glass particles, clay minerals, siliceous microfossils, and some detrital quartz and feldspar.

Bulk sediment chemistry and chemical enrichment factors calculated with respect to the reference sediment indicate that the most important chemical changes occurred at the base of the core from 100 to 124 cm bsf, with strong enrichments in MnO, CaO, P_2O_5, and Fe_2O_3. These enrichments are correlated with the occurrence of authigenic Fe-oxyhydroxide (goethite) and Mn oxide (todorokite and vernadite, at 100 cm bsf), and hydrothermal apatite (110-124 cm bsf). In the upper section of the core from 12 to 70 cm, the sediment is composed of abundant smectite and authigenic phillipsite, and only minor chemical changes can be observed with respect to the reference sediments.

The ubiquitous presence of phillipsite suggests that the entire sedimentary column of core GC50 was first affected by diagenesis. However, below 70 cm bsf, these phillipsites are partially dissolved and Fe oxides occur from 110 to 124 cm, followed

upward by Mn oxides at 100 cm. This transition from Fe to Mn rich sediments can be interpreted in terms of an upward increasing redox potential. PAAS-normalized REE patterns of GC50 sediments present clearly negative Ce and positive Y anomalies inherited from seawater at the base of core GC50. These anomalies decrease upward, which we interpret together with the transition from Fe to Mn-rich sediments by an upward migrating low temperature hydrothermal fluid. Thus, after a first stage of diagenesis, the discharge of a low temperature hydrothermal fluid occurred through the sedimentary column, leading to the precipitation of hydrothermal compounds that are lacking towards the surface.

KEYWORDS: East Pacific Rise; ridge flank; hydrothermalism; alteration; metalliferous deposits; Rare Earth Elements.

1. Introduction

Oceanic metalliferous deposits consisting of assemblages of Fe-Mn oxyhydroxides, zeolites, and clay minerals are efficient scavengers for trace elements such as Ni, Co, Cu, and rare earth elements and Yttrium (REY; Hein et al., 1997; Kuhn et al., 1998). Such deposits result from the precipitation of dissolved metals from seawater, porewater, or hydrothermal fluids and have been classified into three general categories based on their mechanisms of formation (Boles, 1977; Kastner, 1981). The first category of metalliferous deposits is called hydrogenetic and results from basalt alteration by seawater occurring directly after crust accretion followed by oxide precipitation from seawater (Cann, 1979; Humphris et al., 1980; Honnorez, 1981). The second category forms during early diagenetic processes, typically within volcanoclastic deposits as well as in deep-sea red clays (Karpoff, 1989; Karpoff et al., 1992; Aoki and Kohyama, 1998). These deposits usually form at redox boundaries within the sediment or at the sediment-water interface. The third category of deposits precipitates from discharging hydrothermal fluids close to the ridge-axis, or on ridge flanks with a thin sedimentary cover (Honnorez et al., 1983; Buatier et al., 1995; Buatier et al., 2000). These hydrothermal deposits generally occur in volcanically active areas mainly at plate boundaries (spreading centers, fracture zones), while hydrogenetic and diagenetic deposits are formed in tectonically stable areas on old oceanic crust (Usui et al., 1997). The nature and the chemical composition of newly formed minerals related to fluid-sediment interactions reflect the nature of the fluids from which they precipitated (hydrothermal fluids, seawater or mixtures) and local physicochemical parameters such as redox conditions.

We studied metalliferous hemipelagic sediments that were sampled near a off

axis basaltic outcrop, on the eastern flank of the East Pacific Rise (EPR, Fig. 1a). The purpose of this paper is to determine the mineralogical and chemical characteristics of the secondary mineral phases in order to elucidate their mechanism of formation. Special attention will be payed to Fe/Mn ratios, trace metal content, and REY patterns, commonly used to trace the origin of metalliferous deposits (Usui et al., 1997).

2. Regional setting

Metalliferous and hemipelagic sediments were collected by gravity coring during the Ticoflux II expedition in 2002, west of the Nicoya Peninsula, Costa Rica (Fig. 1a). The aim of this expedition was to study the impact of low temperature ridge-flank hydrothermal activity on the cooling rate of the Cocos plate consisting of a 18-24 Ma-old crust (Fisher et al., 2003). The Cocos plate has a complex tectonic history in the Ticoflux II area, comprising basalt crust generated at the EPR (East pacific Rise) at fast spreading rates and at the CNS (Cocos-Nasca Spreading Center) at intermediate spreading rates. The heat-flow measured on EPR generated crust is typically 90% below theoretical heat-flow predicted by the conductive lithosphere model, suggesting that cooling has been strongly accelerated by the circulation of hydrothermal fluids (Vacquier and Sclater, 1967; Von Herzen and Uyeda, 1963; Fisher et al., 2003). In contrast, the heat flow of CNS generated crust is in good agreement with calculated conductive heat-flow values. The Ticoflux cruises focused on the hydrologic processes that determine heat-flow distribution using heat-flow measurements, coring, and seismic surveys. Plate boundaries, seamounts, and basaltic outcrops were the primary targets for sampling, because they are fundamental structures for fluid circulation (Harris et al., 2004).

The results from ODP Hole 1039, drilled in close vicinity (Fig. 1a), document that the sedimentary cover of the Cocos plate is ~450 m thick. The upper 150 m are composed of Pleistocene to Pliocene hemipelagic muds, followed below by Miocene pelagic nanofossil oozes. The sedimentation rate is ~46 m/m.y. for the Pleistocene and 6 m/m.y. for the Pliocene and late Miocene (Silver et al., 1997). However, in the Ticoflux area the nature and the thickness of the sediments vary laterally with seafloor topography, bottom currents, and distance from the continent. In general, the total sediment thickness does not exceed 200 m and the overlying hemipelagic sediment section is thin or absent on the top of seamounts (Spinelli and Underwood, 2004).

The gravity cores studied are from the Dorado outcrop, a 100 m high basaltic seamount from 3150 m water depth (Fig. 1a). Heat flow along the SW slope reached values up to 389 $mW*m^{-2}$, which is much higher than the theoretical range of 95 to 120 $mW*m^{-2}$ calculated for a 18-24 Ma old seafloor (Fisher et al., 2002). Fourteen gravity cores were taken on and around the Dorado outcrop (GC 33 to 43 and GC 49 to 51). The sediments of the area consist of hemipelagic mud in core collected at the base of the seamount and on its southwestern slope, whereas highly altered yellowish brown mud (locally zeolitic) and Mn-oxide occur on its northwestern side (Fisher et al., 2002). Phosphate concentrations and alkalinity values of pore water decrease with depth in some of the cores, consistent with upward flowing fluids with low phosphate concentrations and alkalinity values issued from basalt-seawater interaction (Wheat et al., 1996). This suggests, together with the heat-flow data, that the Dorado Outcrop is a site of active discharge of low temperature hydrothermal fluid (< 65°C).

The location for gravity core GC50 on the northwestern slope of the Dorado outcrop, at 3142 m water depth, was chosen because of the highest heat flow in this area (Fig. 1b, at 9°05.044 °N - 87°05.929 °W). This 138 cm long core consists of a mottled

mixture of dark yellowish brown zeolitic clay and yellowish brown mud from 12 to 70 cm below seafloor (bsf), some up to 6 cm thick layers and patches of oxides with phosphates and altered zeolites from 70 to 124 cm bsf. Scattered fragments of glassy basalt at the base of the core indicate the proximity to the basalt-sediment interface (Fig. 2). Our study is focused on core GC50 and for comparison we present data from the adjacent cores GC38, GC42, and GC43 (Fig. 1b). These latter cores are composed of hemipelagic mud with no metalliferous deposits. In the following, we consider that these samples, called "reference sediments", represent the unmineralized sediment of core GC50.

3. Materials and methods

Five samples of bulk sediments from core GC50 (at 2, 30, 52, 100 and 110 cm bsf) representative of each lithologic level, and two bulk reference sediments from neighboring cores (GC42 114 cm bsf and GC38 90 cm bsf) were analyzed by X-ray diffraction (XRD) and observed by scanning and transmission electron microscopy (SEM and TEM).

XRD analyses of bulk sediment samples were conducted at the Geological Institute of the University of Neuchâtel with a Sintag 2000 diffractometer using Cu Kα radiation with 2θ slit varying between 0 and 60° at a scan speed of 0.5°/min, 45 kV/*18 mA*, 0.1°-1° slits. Samples were prepared following the procedure of Kübler (1987). About 800 mg of sediment was ground to powder, pressed at 20 MPa in a powder holder, covered with a blotting paper, and analyzed. The relative abundances of minerals were estimated qualitatively, based on peak heights without interferences. A semi-quantitative evaluation of the X-ray diffraction data was not possible because of

the abundance of amorphous siliceous fossils and volcanic glass. The clay minerals were identified on oriented samples of <2 μm and 2-16 μm fractions collected on glass slides, after air-drying, and again after ethylene-glycol treatment. To identify more precisely the diffraction peak positions, XRD patterns were decomposed into elementary Gaussian curves using the McDiff program.

Detailed petrographic observations of freshly broken and carbon-coated sample surfaces were performed using a scanning electron microscope (SEM Jeol 5600 operating at 20 kV) equipped with a X-ray EDX Fondis detector (Centre Commun de Microscopie, Université de Franche Comté, Besançon). EDX analysis provided qualitative chemical compositions. For TEM analyses, sediments were stored at 5 °C immediately after sampling. Selected samples were then impregnated in a Spurr resin according to the method of Tessier (1984) and Elsass et al. (1998), cut with a diamond knife on an ultramicrotome, and collected on carbon coated Cu grids. We used a Jeol 1260 at 120kV (CCME, Université de Franche Comté, Besançon) and a Philips CM30 at 300kV equipped with a EDAX detector (CCM, Université de Lille 1).

Chemical analyses were performed on 11 bulk samples from core GC50 and four reference sediments (38GC90, 38GC225, 42GC114 and 43GC88-90 cm bsf), at the Centre de Géochimie de la Surface at CNRS Strasbourg (France). The samples were ground in an agate mill, dried at 110 °C, calcinated at 1000 °C, melted with a mixture of lithium tetraborate, and dissolved in a glycolated solvent for analysis (Samuel et al., 1985). Major element contents (in wt.% oxides), and trace and rare-earth element contents (in ppm) were determined with a precision of ± 5% by ICP-AES (Jobin Yvon) and ICP-MS (VG Plasmaquad PG2+).

4. Results

4.1. Sedimentology and mineralogy

The reference sediments are olive gray hemipelagic muds mainly composed of siliceous microfossils (radiolarians, diatoms, sponge spicules), clay minerals, and volcanic glass particles, according to SEM observations (Fig. 3a). XRD patterns (Fig. 4) show that the clay minerals are smectites, and also reveal the presence of halite, quartz, and feldspar.

At the top of the core (2 cm bsf), a nodule of about 5 cm in diameter was collected (Fig. 2). According to SEM observations, it consists of siliceous microfossils encrusted by black oxides (Fig. 3b). Microfossils seem to have served as a framework for cementation by oxides rich in Mn and Fe as confirmed by the chemical data (Table EA-1).

Sediment samples from mid-core (12-70 cm bsf) are composed of yellowish brown mud containing a mottled mixture of zeolites and clay minerals (Fig. 3c). All samples between 12 and 70 cm bsf present similar XRD patterns. A typical example from 52 cm bsf is shown in Fig. 4. The XRD data allowed to identify the zeolites as phillipsite (major reflections at 3.19 Å and 7.17 Å). This is in agreement with qualitative EDX data from individual crystals, yielding peaks for Si, Al, Na, and K. SEM images of bulk sediment show euhedral prismatic crystals with a size of 20 μm to 1 mm (Fig. 3c), often concentrated in clusters that fill cavities and voids in the sediment. The XRD data furthermore reveal the presence of barite (BaSO4) (Fig. 4). Phillipsite and barite represent the dominant mineral phases in this part of core GC50 and they are accompanied by minor portions of quartz, halite and clay minerals.

The diffraction pattern of the oriented <2 μm fraction displays a large and asymmetric peak between 5 and 9 °2θ (Fig. 5b), in the air-dried sample at 52 cm bsf. A simulated XRD pattern reproduces a comparable asymmetric peak by superposition of two gaussian curves at respectively 7.3° 2θ (12.6 Å, the most intense) and 6.4° 2θ (13.6 Å, Fig. 5b). After glycolation, the observed peaks are shifted towards lower 2θ angles: the most intense peak is at 5.2° 2θ (16.8 Å) and the second peak at 5.9° 2θ (15 Å). The shift of the 001 reflection from 12.6 Å for air-dried sample to 16.8 Å after glycolation is characteristic for smectite having one water layer in the interlayer position (Deer et al., 1992). The second reflection at 13.6 Å shifted to 15 Å after glycolation corresponds to less expandable clay minerals and can be attributed to irregular mixed-layer chlorite-smectite (Holtzapffel, 1985). The diffraction pattern of the oriented <2 μm fraction of the reference sediment shows a similar asymmetric peak between 5 and 9 °2θ (Fig. 5a). As for the GC50 sediment, this asymmetric peak can be reproduced by superposition of two gaussian curves which are shifted to 16.9 Å and 15 Å when glycolated. The < 2 μm fraction of the reference sediment is thus similar to the upper part of core GC50, mainly composed of smectite and mixed-layer chlorite-smectite.

At 100 cm bsf, a black layer is mainly composed of Fe-Mn oxyhydroxide, phosphate and phillipsite (Fig. 4). XRD analyses of this sample (GC50 100 cm) show large peaks at 9.68 Å and 4.80 Å characteristic of todorokite and/or 10Å-vernadite (Fig. 4). Todorokite is a manganate with a tunneled-structure and an octahedral sheet of about 10 Å with a cross row octahedral chain running along the b axis. 10Å-vernadite is a disordered phyllomanganate with a 10 Å-thick octahedral sheet layer related to the presence of water and cations within the interlayer (Bodeï et al., 2007; Manceau et al., 2007). These oxyhydroxides show micro-hemispheroidal structures or filament textures under the SEM (Fig. 3d). The spheroids are 10 to 30 μm in diameter and have a

honeycomb structure formed by the aggregation of flaky particles of about 2 μm in size. These aggregates seem to have grown on zeolite surfaces (Fig. 3e). Under the TEM, the diameter of the spheroids varies from 5 to 25 μm with a systematic mineralogical zonation (Fig. 6a). The size and morphology of the individual oxide particles vary from the center to the edge: the center is composed of poorly crystallized nanometric particles of phyllomanganate embedded within better crystallized flakes of 10Å-vernadite, whereas elongated laths of todorokite occur towards the edge of the microconcretions.

Figure 4 shows the XRD pattern from 110 cm bsf as a typical example of the GC50 sediments below 100 cm bsf. The pattern displays major reflections at 2.80 Å and 2.71 Å corresponding to the major reflections of fluorapatite and hydroxyapatite. Phillipsite is also present in this section as well as quartz and halite. SEM observations confirm the presence of well crystallized authigenic phosphates occurring as aggregates of small euhedral crystals of about 0.7 μm (Fig. 3f). On TEM images, these euhedral crystals display the typical hexagonal morphology of apatite when observed along the 001 zone axis (Fig. 6b). In this part of the core, Fe oxides are also present often on phillipsite surfaces. Their poor cristallinity did not allow their characterization by XRD. However, TEM images show that aggregates of Fe-rich nanoparticles, with common cellular texture, display electron diffraction diagrams with two broad circular reflections at 4.19 Å and 2.44 Å, which could correspond to the (101) and (111) reflections of goethite (Fig. 6b).

Associated to these major phases, XRD diffractograms indicate the presence of quartz and halite in all core GC50 samples (Fig. 4). The occurrence of halite is certainly related to precipitation during sample drying.

4.2. Chemical data

4.2.1 Major and trace elements

The bulk chemistry of the reference sediment (GC38, GC42, and GC43) is characterized by about 55 % SiO_2, 15 % Al_2O_3, and low contents of CaO (~ 2%), P_2O_5 (~ 0.2%), and MnO (~ 0.13%) (Table EA-1). The altered sediments from core GC50 contain lower Al_2O_3 and SiO2 concentrations, but relatively high CaO, MnO, and P_2O_5 contents, especially below 70 cm bsf. Compared with the reference sediment, GC50 samples also present high Ba, Ni, Co and Cu contents. In the non-indurated Mn-rich horizon from 100 cm bsf, the Ni and Cu contents are higher than those in hydrothermal crusts from the Valu Fa ridge and approach concentrations typical for Mean Pacific hydrogenous crusts (Hein et al., 1997). The metalliferous surface nodule from 2 cm bsf presents a relatively high Mn concentration. However, its Mn/Fe ratio (4.30) is lower than in the non-indurated Mn horizon at 100 cm bsf (16.73) (Table EA-1).

In a ternary Al-Fe-Mn diagram (Dymond and Corliss, 1973; Toth, 1980), all reference samples are almost Mn-free with an Al/Fe mass ratio of about 1.32 (Fig. 7). In contrast, samples from core GC50 are shifted towards the Mn apex with increasing depth. Four groups can be distinguished. The first group (I) consists of samples from 12-38 cm bsf and is characterized by weak Mn enrichment. A second group (II) with a slightly greater Mn enrichment consists of samples from 52 to 70 cm bsf. The third group (III) is defined by the samples from 2 and 100 cm bsf, which are characterized by a strong Mn enrichment and low Fe concentrations. Finally, the fourth group (IV) includes the basal sediments from 110 and 124 cm bsf. This latter group does not follow the general trend and has Mn concentrations similar to the second group, but shifted towards the Fe apex (Fig. 7).

To permit a more direct comparison, we have calculated enrichment factors for all elements in GC50 samples, with respect to the reference sediment.

4.2.2 Enrichment Factors

The enrichment factor E_i, used to quantify the chemical variations within core GC50, is defined as

$E_i = (C_i/C_{Al})$sample / (C_i/C_{Al})reference sediment (Li, 1982)

whereas C_i stands for the concentration of an element i and C_{Al} to the concentration of Al. The normalization with respect to Al is used because Al is considered to be the most immobile major element. As reference sediment we use as previously the average of the four samples from cores GC38, GC42, and GC43.

E_i is close to 1 for SiO_2, K_2O, Na_2O, and MgO, suggesting that these elements remained almost unchanged during alteration (Fig. 8a). For sediments above 100 cm bsf, the enrichment factor for Fe_2O_3 is also around 1, whereas the values for CaO, P_2O_5 and MnO are bigger than 1 and increase with depth (Fig. 8b). Trace elements (Ba, Ni, Co and Cu) are also slightly enriched in this section above 100 cm (Fig. 8c). The highest Ei value of about 1000 is found for MnO in the non-indurated Mn layer at 100 cm bsf (Fig. 8b). The Ei values for Ni and Co have similar depth evolution as MnO and reach values of about 100 at 100 cm bsf (Fig. 8c). The Ei values for P_2O_5, Fe_2O_3, and CaO evolve similarly with depth reaching, in contrast to MnO, their maximum values not at 100 cm bsf but in the two deepest samples at 110 and 124 cm bsf.

4.2.3 Rare Earth Elements and Yttrium (REY)

The PAAS-normalized REY patterns of the reference samples are almost flat except for the distinct positive Eu anomaly and a slight enrichment of the heavy Rare Earth Elements (HREE, Gd-Lu) (Fig. 9). Reference sample REY concentrations are distinctly lower than those in GC50 sediments. This is confirmed by the calculated enrichment factor for neodymium, showing a slight increase with depth in the core from 2 to 6 (Fig. 8c). Except for a positive Eu anomaly, the patterns from core GC50 are very similar to seawater, with negative Ce and positive Y anomalies, and a HREE enrichment (Fig. 9b,c). Negative Ce anomaly values ($Ce/Ce^* = 3Ce_N/[2La_N+Nd_N]$) are between 0 and 1, whereas positive Eu anomaly values ($Eu/Eu^* = Eu_N/[\sqrt{(Sm_N*Gd_N)}]$) are above 1 (Table EA-2). In core GC50, Eu/Eu* and Ce/Ce* values decrease regularly from the top to bottom achieving almost seawater-like values at the base of the core (Fig. 10, Table EA-2). In contrast, the surface nodule is characterized by a REY pattern that differs from the other samples by having a positive Ce anomaly, a negative Y anomaly, and lack of a HREE enrichment (Fig. 9a).

5. Discussion

5.1 Origin of the authigenic components

Mineralogical observations demonstrate the presence of authigenic minerals in core GC50 suggesting that the pristine sediment has been modified by fluid-sediment interaction. The authigenic phases include phillipsite and barite especially from 12 to 70 cm bsf, then apatite, and Mn and/or Fe oxides from 100 to 124 cm bsf.

The surface nodule, composed of a mixture of Mn oxides and fragments of microfossils, is chemically distinct from the underlying sediment. Its PAAS-normalized REY pattern precludes, together with the enrichment in Ni and Cu, a hydrothermal

origin (Usui et al., 1997; Dekov et al., 2003). In contrast, in particular the positive Ce anomaly is rather indicative for hydrogenetic Mn nodules (Usui et al., 1997). However, the Co concentration is below values typical for Mean Pacific hydrogenetic crusts (Hein et al., 1997; Table EA-1). Diagenetic nodules formed in oxic sediments usually have high concentrations in Mn, Cu, and Ni, and are particularly enriched in Cu and Ni. Such diagenetic nodules are furthermore characterized by Mn/Fe ratios between 2.5 and 5 (Dymond et al., 1984; Takematsu et al., 1989). The Mn/Fe ratio of our surface nodule of 4.3 falls within this range. However, this surface nodule is exposed to the water column and may therefore also include a weak hydrogenetic component as suggested by its Co and Fe concentrations that are higher than in typical diagenetic nodules, and by the positive Ce anomaly (Verlaan et al., 2004; Usui et al., 1997).

The sediment from 12 to 70 cm bsf is only slightly different from the reference sediment (Figs. 7). The clay fraction is in both cases composed of smectite associated with some chlorite/smectite mixed layers. Smectite is a common detrital mineral in deep-sea sediments, but it has also been described as an alteration product of volcanic glass (Chamley, 1989). According to Spinelli and Underwood (2004), smectite is ubiquitous in hemipelagic mud and olive brown clay off the Nicoya Peninsula. These authors described a sediment mainly composed of smectite including probably some illite in a disordered mixed-layer structure, and concluded from this a detrital rather than a diagenetic origin from the alteration of volcanic glass. SEM and TEM investigations did not show textural evidence for the presence of authigenic smectite. Furthermore, smectite is present in both reference and GC50 sediments. For all these reasons we conclude that smectite in core GC50 is of detrital origin.

The barite content found in core GC50 is much higher than in the reference

samples and also much higher than can be anticipated from regional organic matter fluxes (Dymond and Collier, 1996). Therefore it is unlikely to be of biogenic origin. The barite from 12 to 70 cm in core GC50 may therefore be of hydrothermal origin (Bonatti et al., 1972; Dymond et al., 1992). Immediately below this interval, the highest Ba concentration of core GC50 occurs in the Mn-oxides rich layer at 100 cm. However, no barite could be identified in this sample (Fig. 4 and 8). Beneath this level occur no other enrichments of Ba or barite. In conclusion, the occurence of hydrothermal barite above the large Ba enrichment of the Mn oxides layer reflects a more complex origin of the GC50 sediment.

The major mineralogical difference between the sediment from the upper part of core GC50 and the reference sediment is the abundance of phillipsite. Phillipsite is a zeolite group mineral that forms in marine sediments mainly by alteration of volcanic glass (Hay, 1964; Sheppard and Fitzpatrick, 1989). On SEM images, phillipsite fills cavities and voids within the sediment underlining that this mineral is of authigenic origin, and can be interpreted as progressive dissolution and replacement of volcanic glass particles (Burns and Burns, 1978). An additional contribution of silica from siliceous tests is probable. The dissolution of siliceous organisms, leading to a strong Si enrichment, normally promotes the formation of clinoptilolite rather than phillipsite (Stonecipher, 1976; Petzing and Chester, 1979). However, even if SEM observations show that siliceous microfossils present in the reference sediment have disappeared in core GC50, the enrichment factors (Ei) for SiO_2 always remain close to 1 all along the sedimentary column (Fig. 8). Moreover, clinoptilolite is often associated with calcareous sediments and high sedimentation rates, whereas in this study zeolites are formed in volcanic and siliceous sediments with a low sedimentation rate. These environmental factors are generally associated to the formation of phillipsite

(Stonecipher, 1976). We can thus suggest that in this particular environmental context the dissolution of volcanic glass particles and probably siliceous microfossils leads to the formation of phillipsite rather than clinoptilolite.

In summary, in the upper part of core GC50 authigenic phillipsite is probably related to early diagenetic processes whereas most of the smectite, also present in the reference samples, is probably of detrital origin.

Below 70 cm bsf, the most important modifications that affected the sediment are strong enrichments in MnO, CaO, P_2O_5, and Fe_2O_3 (Fig. 8b), leading to the precipitation of Fe oxide (goethite), Mn oxide (todorokite and 10Å-vernadite), and apatite. SEM observations show that Mn and Fe oxides encrust zeolite crystals suggesting that their precipitation postdates that of phillipsite. Moreover, TEM observations of the Mn oxides at 100 cm bsf revealed the presence of Mn microconcretions with a particular structure suggesting that the phyllomanganates of the vernadite family precipitated first on zeolites, followed by todorokite (Fig. 6a). Such a coexistence of todorokite and 10Å-vernadite is common for marine low temperature hydrothermal deposits (Usui et al., 1986; Hein at al., 1997; Koschinsky and Hein, 2003). The high concentrations of Ni, Co, and Cu in this sample can be explained by scavenging of these elements by the Mn oxides (Marchig et al., 1999). Dissolution of biogenic siliceous components is a possible source of Ni, Co, and Cu (Burns and Burns, 1978).

Apatite has only been detected in the deepest part of the core, where the enrichment factors (Ei) for CaO and P_2O_5 are highest (Fig. 8). However, the strong correlation between the Ei values of CaO and P_2O_5 over the entire core ($r^2 = 0.99$) suggests that small amounts of apatite, not detected by X-ray diffraction and

microscopy, may also be present at smaller depth. The apatite observed in the deepest part of the core occurs as aggregates of idiomorphous euhedral crystals of about 0.7μm (Figs. 3f and 6b) and is thus of authigenic origin. Phosphorous in marine sediments is mainly derived from the decomposition of organic matter, a process that is controlled by biologic activity and the availability of oxygen within the sediment. The released phosphorous can directly precipitate as authigenic P-bearing minerals or be integrated into Fe oxyhydroxides (Froelich et al., 1982; Berner et al., 1993). Therefore, the phosphorus cycle can be closely related to the stability of Fe oxyhydroxides, which is directly redox controlled (Krom and Berner, 1980). Consequently, dissolved P can be scavenged by Fe oxihydroxides under oxic conditions, then be remobilized by the reductive dissolution of Fe oxhydroxides during burial. The released P may return to the ocean or remain within the sediment and contribute to the formation of authigenic phosphate minerals (Cha et al., 2005). Hydrothermal processes, especially low temperature systems, are considered to be a major sink for P in the oceans (Froehlich et al., 1982; Wheat et al., 1996). In such systems, the relative apatite enrichment can be of organogenic origin (fish bone debris) or result from precipitation of hydrothermal apatite as described by Marchig et al. (1999) for sediments from the Peru basin. These authors found that P_2O_5/Y ratios were higher in hydrothermal apatite than in adjacent biogenic apatite. They explained this difference by the absence of a complete reequilibration of hydrothermal apatite with seawater. In the samples from the deeper part of core GC50, P_2O_5 reaches 12 %, and Y 130 ppm (Table EA-1 and EA-2), yielding a P_2O_5/Y ratio that is highly above the regression line of biogenic apatite, whereas the sample from above 100 cm bsf plots together with the reference samples on the regression line (Fig. 11). We thus conclude that apatite observed at the base of core GC50 is likely of hydrothermal origin. The precipitation of authigenic phosphate

minerals rather than incorporation of P in iron oxyhydroxides occurs, probably because of the high hydrothermal P flux under the reducing conditions at the base of the core.

5.2 Indications for an upward fluid flow

The chemical enrichment factors presented in section 4.2.2 show that the highest Ei values in core GC50 occur below 70 cm with enrichment factor up to 1000 for MnO at 100 cm (Fig. 8). By comparison, the enrichment factors remain close to 1 in the upper part of the core, suggesting that authigenic phillipsite occurring above 70 cm bsf is of early diagenetic origin and derived from volcanic glass particles and possibly biogenic tests. These data show that the strongest chemical changes occured in the deepest sediments, below 70 cm bsf.

The enrichment factors for MnO, CaO and P_2O_5 are >1 above 70 cm bsf, and continually increase up to their maximum values below 70 cm. The slight enrichment from 12 to 70 cm suggests that small amounts of phosphate and Mn oxides are also present in the upper part of the core. The Nd content follows the same trend in this section (Fig. 8c), and is better correlated with P_2O_5 ($r^2 = 0.724$) than with MnO ($r^2 = 0.502$), suggesting that the phosphate is the main REY carrier phase above 100 cm bsf.

Apatite, Fe oxides and Mn oxides are the major authigenic phases in the basal part of the sedimentary column. The Ei values for P_2O_5 and Fe_2O_3 are highest for the samples at 110 and 124 cm bsf, whereas MnO reaches its maximum value at 100 cm bsf. This succession between Fe_2O_3 and MnO can be explained by an upward increasing redox potential where the oxidation of Fe^{2+} to Fe^{3+} occurs at an Eh of about 0 mV and Mn^{2+} oxidizes to Mn^{4+} above 400 mV. Such an upward increasing redox potential is typical for hydrothermal systems and can be explained by the progressive mixing of a

reduced ascending fluid with a more oxygenated porewater towards the sediment-seawater interface (Hein et al., 1994).

To confirm the probable occurrence of an ascending hydrothermal fluid, we focus on REY distribution patterns commonly used to determine the origin of metalliferous deposits (Elderfield and Greaves, 1982). All GC50 samples, excluding the surface nodule, show PAAS-normalized REY patterns characteristic for seawater, except for a strong positive Eu anomaly (Fig. 9b and c). The strong negative Ce anomaly in seawater is due to its quadrivalent oxidation state leading to a preferential removal of Ce from seawater with respect to the other REY which are all trivalent. The pronounced enrichment of the heavy REEs relative to the light REEs is due to the greater stability of HREE complexes in seawater (Elderfield and Greaves, 1982). The REY patterns of low-temperature hydrothermal fluids strongly resemble seawater patterns (Alt, 1988), because they result from the infiltration and the migration of seawater through fractured oceanic basalts with only limited seawater-basalt interaction due to the low temperatures and short residence times (Wheat et al., 1996). The positive Eu anomaly observed in GC50 samples is also present in the reference sediment. Europium commonly substitutes for Sr in feldspars, notably Ca-plagioclases (McLennan, 1989). The positive Eu anomaly of the reference sediment can thus be explained by the presence of plagioclase identified by XRD (Fig. 4) and commonly associated to volcanic glass (Marchig et al., 1999). However, feldspar is rare or absent in GC50 sediment. Alternatively, zeolites, which are the dominant mineral phase in the upper part of core GC50, could be the Eu carrier since they probably derive from the alteration of volcanic glass particles and the breakdown of plagioclase (Laverne et al., 1996). Consequently, the downward decreasing Eu/Eu* anomaly in GC50 core could be explained by the progressive alteration of zeolites and/or plagioclase with depth.

The seawater-like REY distribution patterns of the GC50 sediments confirm an exchange with a low-temperature hydrothermal fluid. The upward decreasing negative Ce and positive Eu anomalies demonstrate furthermore that this hydrothermal influence was strongest at the base and decreased upward.

6. Summary and conclusions

Mineralogical and chemical data define depth-related trends of sediment alteration in gravity core GC50 recovered from the western edge of a seamount east of the East Pacific Rise, at about 9°N. The sedimentary sequence of the core can be subdivided into three units :

- The surface nodule (GC50 2 cm) is mineralogically and chemically distinct from the sediment of the core. This Mn-Fe oxide nodule shows a REY pattern with a positive Ce anomaly precluding a hydrothermal origin. Its high Ni and Cu contents and a Mn/Fe ratio between 2.5 and 5 suggest a diagenetic origin. However, a weak hydrogenetic contribution from the overlying seawater leads to a low enrichment in Co and Fe.
- In the middle part of the sedimentary column (from 12 to 70 cm bsf), chemical exchanges were limited to the formation of diagenetic phillipsite. However, these sediments show a negative Ce anomaly (weaker than in the basal sediments) and a REY pattern similar to sediments of low temperature hydrothermal origin, suggesting a hydrothermal overprint with a low enrichment in phosphate and Mn oxides.
- In the basal sediments (below 70 cm bsf), the Fe/Mn fractionation and

the REYs with a seawater pattern are typical of alteration produced by a reduced ascending fluid of low temperature. The resulting hydrothermal precipitates correspond to authigenic apatite, Fe oxide (goethite), and a mixture of todorokite and 10Å-vernadite enriched in Ni and Cu probably due to the dissolution of the biogenic siliceous components.

This mineralogical and chemical study of the GC50 core suggests the occurence of an ascending hydrothermal fluid of low-temperature on "Dorado high". This discharge started after a early stage of diagenesis that affected the entire sedimentary column, and lead to the precipitation of hydrothermal minerals that decrease upcore.

7. Acknowledgements

The authors thank Nicolas Rouge (CCME, Besançon) who helped with SEM analyses, and René Boutin (Centre de Géochimie de la Surface, CNRS Strabourg) for ICP-AES and ICP-MS analyses. This research was financially supported by the GDR Transmet (MB) and the NSF grant OCE 98-19454 (GW).

8. References

Alibo, D.S, Nozaki, Y., 1999. Rare Earth Elements in seawater: Particle association, shale-normalization, and Ce oxidation. Geochim. Cosmochim. Acta 63, 363-372.

Alt, J.C., 1988. Hydrothermal oxide and nontronite deposits on seamounts in the Eastern Pacific. Mar. Geol. 81, 227-239.

Aoki, S., Kohyama, N., 1998. Cenozoic sedimentation and clay mineralogy in the Northern part of the Megallen Trough, Central Pacific basin. Mar. Geol. 148, 21-37.

Berner, R.A., Ruttenberg, K.C., Ingall, E.D., Rao, J.L., 1993. The nature of phosphorus burial in modern marine sediments, in: Wollast, R., Mackenzie, F.T., Chou, L. (Eds.), Interactions of C, N, P and S Biogeochemical Cycles and Global Change. Springer-Verlag, New York, pp. 365-378.

Bodeï, S., Manceau, M., Geoffroy, N., Baronnet, A., Buatier, M., 2007. Formation of todorokite from vernadite in Ni-rich hemipelagic sediments. Geochim. Cosmochim. Acta, in press.

Boles, J.R., 1977. Zeolites in deep-sea sediments. Mineralogy and Geochemistry of Natural Zeolites. Mineral. Soc. of Am. Short Course Notes 4, 137-163.

Bonatti, E., Kraemer, T., Rydell, H.S., 1972. Classification and genesis of submarine iron-manganese deposits. Ferromanganese deposits on the Ocean Floor: palisades, N.Y. (Lamont-Doherty Geol. Observ. Columbia Univ.), 149-166.

Buatier, M., Früh-Green, G.L., Karpoff, A.M., 1995. Mechanisms of Mg-phyllosilicate formation in a hydrothermal system at a sedimented ridge (Middle Valley, Juan de Fuca). Contr. Mineral. Petrol. 122, 134-151.

Buatier, M., Monnin, C., Frü-Green, G., Karpoff, A.M., 2000. Fluid-sediment interactions related to hydrothermal circulation in the Eastern Flank of the Juan de Fuca Ridge. Chem. Geol. 175, 343-360.

Burns, V.M., Burns, R.G., 1978. Authigenic todorokite and phillipsite inside deep-sea manganese nodules. Am. Mineral. 63, 827-831.

Cann, J.R., 1979. Metamorphism in the ocean crust, Deep Drilling Results in the Atlantic Ocean: Ocean Crust., American Geophysical Union, Washington, D.C.

Cha, H.J., Lee, C.B., Kim, B.S., Choi, M.S., Ruttenberg, K.C., 2005. Early diagenetic redistribution and burial of phosphorus in the sediments of the southwestern East Sea (Japan Sea). Mar. Geol. 216, 127-143.

Chamley, H., 1989. Clay Sedimentology, ed. Springer-Verlag, Berlin Heidelderg, pp. 291-329.

Chukhrov, F.V., Gorshkov, A.I., Sivtsov, A.V., Berezovskaya, V.V., 1978. Structural varieties of todorokite. Izvestia Akademia Nauk, SSSR, Ser. Geol. 12, 86-95.

Chukhrov, F. V., Sakharov, B. A., Gorshkov, A. I., Drits, V. A., Dikov, Y. P., 1985. Crystal structure of birnessite from the Pacific Ocean. International Geology Review (translated from Investiya Akademie Nauk, SSSR, Seriya Geologicheskaya, 8, 66-73) 27, 1082-1088.

Deer, D.A., Howie, R.A., Zussman, J., 1992. An introduction to the rock-forming minerals. 2nd edition. Longman Scientific & Technical, London, 696 pp.

Dekov, V.M., Marchig, V., Rajta, I., Uzonyi, I., 2003. Fe-Mn micronodules born in the metalliferous sediments of two spreading centers: the East Pacific Rise and Mid-Atlantic Ridge. Mar. Geol. 199, 101-121.

Dymond, J., Corliss, J.B., 1973. Origin of metalliferous sediments from the Pacific. Ocean. Geol. Soc. Am. Bull. 84, 3355-3372.

Dymond, J., Lyle, M., Finney, B., Piper, D.Z., Murphy, K., Conard, R., Pisias, N., 1984. Ferromanganese nodules from MANOP sites H, S and R-control of mineralogical and chemical composition by multiple accretionary processes. Geochim. Cosmochim. Acta 48, 931-949.

Dymond, E., Suess, E., Lyle, M., 1992. Barium in deep sea sediments: A geochemical proxy for paleoproductivity. Paleoceanography 7, 163-181.

Elderfield, H., Greaves, M.J., 1982. The Rare Earth Elements in sea water. Nature 296, 214-219.

Elsass, F., Beaumont, A., Pernes, M., Jaunet, A.M., Tessier, D., 1998. Changes in layer organization of Na and Ca exchanged smectite during solvent exchange for embedment in resin. Can. Mineral. 36, 1325-1333.

Fisher, A., Buatier, M., Costa, P., Ellsworth, C., Friedmann, P., Harris, R., Hasterok, D., Hernandez, B., Hutnak, M., Jones, M., MacKnight, B., Moser, C., Parsons, W., Silver, E., Spinelli, G., Stein, C., Underwood, M., Wheat, G., 2002. The thermal state of 20-25 Ma lithosphere subducting at the Costa Rica Margin: implications for hydrogeology, fluxes and seismogenic zone. Preliminary Cruise Report, Ticoflux 2 Expedition, 28 pp.

Fisher, A.T., Stein, C.A., Harris, R.N., Wang, K., Silver, E.A., Pfender, M., Hutnak, M., Cherkaoui, A., Bodzin, R., Villinger, H., 2003. Abrupt thermal transition reveals hydrothermal boundary and role of seamounts within the Cocos Plate. Geophys. Res. Lett. 30, 1-4.

Froelich, P.N., Bender, M.L., Luedtke, N.A., Heath, G.R., DeVries, T., 1982. The marine phosphorus cycle. Amer. J. Sci. 282, 474-511.

Harris, R.N., Fisher, A.T., Chapman, D., 2004. Fluid flow through seamounts and implications for global mass fluxes. Geology 32 (8), 725-728.

Hay, R.L., 1964. Phillipsite of saline lakes and soils. Am. Mineral. 49, 1366-1387.

Hein, J.R., Hsueh-Wen, Y., Gunn, S.H., Gibbs, A.E., Chung-Ho, W., 1994. Composition and origin of hydrothermal ironstones from central Pacific seamounts. Geochim. Cosmochim. Acta 58, 179-189.

Hein, J.R., Koschinsky, A., Halbach, P., Manaheim, F.T., Kang, J.K., Lubick, N., 1997.

Iron and manganese oxide mineralization in the Pacific. In: Nicholson, K., Hein, J.R, Bühn, B., Dasgupta, S. (Eds.), Manganese Mineralization: Geochemistry and Mineralogy of Terrestrial and Marine Deposits. Geol. Soc. London Spec. Publ. 119, 123-138.

Holtzapffel, T., 1985. Les minéraux argileux. Préparation, analyse diffractométrique et détermination. Soc. géol. du nord 12, 67-91.

Honnorez, J., 1981. The aging of the oceanic crust at low temperature, in: C. Emiliani (Eds), The oceanic lithosphere. Wiley and Sons, New York, pp. 525-597.

Honnorez, J., Karpoff, A.M., Trauth-Badaut, D., 1983. Sedimentology, mineralogy and geochemistry of green clay samples from the Galapagos hydrothermal mounds, Holes 506, 506C and 507D Deep Sea Drilling Project Leg 70. Initial Reports DSDP, US Gov. Print. Office, Washington, D.C., pp. 221-224.

Humphris, S.E., Thompson, R.N., Marriner, G.F., 1980. The mineralogy and geochemistry of basalt weathering, Holes 417A and 418A. Initial Reports DSDP, US Gov. Print. Office, Washington, D.C., pp. 1201-1218.

Karpoff, A.M., 1989. Les faciès pélagiques condensés des Océans Pacifique et Atlantique: témoins des grandes crises géodynamiques. DOc. Es Sci. Thesis, ULP, Strasbourg, France.

Karpoff, A.M., France-Larnord, C., Lothe, F., Karcher, P., 1992. Miocene tuff from

Mariana Basin, Leg 129, Site 802: a first deep-sea occurence of thaumasite. Proceeding ODP, Sci. Results, 129, College Station, Texas, pp. 119-135.

Kastner, M., 1981. Authigenic silicates in deep-sea sediments: formation and diagenesis, in: W.a. Sons (Eds), The Oceanic Lithosphere. The Sea. Wiley F.A. Mumpton, New York, pp. 915-980.

Koschinsky, A., Hein, J.R., 2003. Uptake of elements from seawater by ferromanganese crusts: solid-phase associations and seawater speciation. Mar. Geol. 198(3-4), 331-351.

Krom, M.D., Berner, R.A., 1980. The diffusion coefficients of sulfate, ammonium, and phosphate ions in anoxic marine sediments. Limnol. Oceanogr. 25, 327-337.

Kübler, B., 1987. Cristallinité de l'illite, méthodes normalisées de préparations, méthodes normalisées de mesures. Cahier de l'institut de Géologie de Neuchâtel, Ser. ADX 1, pp. 13.

Kuhn, T., Bau, M., Blum, N., Halbach, P., 1998. Origin of negative Ce anomalies in mixed hydrothermal-hydrogenetic Fe-Mn crusts from the Central Indian Ridge. Earth Planet. Sci. Lett. 163, 208.

Laverne, C., Belarouchi, A., Honnorez, J., 1996. Alteration mineralogy and chemistry of the upper oceanic crust from Hole 896A, Costa Rica Rift. Proc. ODP, Sci. Results 148, 151-170.

Li, Y.H., 1982. Interelement relationship in abyssal Pacific ferromanganese nodules and associated pelagic sediments. Geochim. Cosmochim. Acta 46, 1053-1060.

Manceau, A., Lanson, M., Geoffroy, N., 2007. Natural speciation of Ni, Zn, Ba, and As in ferromanganese coatings on quartz using X-ray fluorescence, absorption, and diffraction. Geochim. Cosmochim. Acta 71, 95-128.

Marchig, V., Von Stackelberg, U., Wiedicke, M., Durn, G., Milovanovic, D., 1999. Hydrothermal activity associated with off-axis volcanism in Peru Basin. Mar. Geol. 159, 179-203.

McLennan, S.M., 1989. Rare Earth Elements in sedimentary Rocks: influence of provenance and sedimentary processes, Geochemistry and mineralogy of Rare Earth Elements. Reviews in Mineralogy, Mineral. Soc. Am., Washington, D.C., pp. 169-225.

Petzing, J., Chester, B., 1979. Authigenic marine zeolites and their relationship to global volcanism. Mar. Geol. 29, 253-271.

Samuel, J., Rouault, R., Besnus, Y., 1985. Analyse multiélémentaire standardisée des matériaux géologiques en spectrométrie d'émission par plasma par couplage inductif. Analusis 13, 312-317.

Sheppard, R.A., Fitzpatrick, J.J., 1989. Phillipsite from silicic tuffs in saline, alkaline-

lake deposits. Clays Clay Miner. 37, 243-247.

Silver, E., Kimura, G., Blum, P., 1997. Costa Rica Accretionary wedge, Sites 1039-1043. Proceedings ODP. Preliminary Report, 170. College station, Texas, pp. 11-16.

Spinelli, G.A., Underwood, M.B., 2004. Character of sediments entering the Costa Rica subduction zone: Implications for partitioning of water along the plate interface. The island Arc 13, 432-451.

Stonecipher, S.A., 1976. Origin, distribution and diagenesis of phillipsite and clinoptilolite in deep-sea sediments. Chem. Geol. 17, 307-318.

Takematsu, N., Sato, Y., Okabe, S., 1989. Factors controlling the chemical composition of marine manganese nodules and crusts. Mar. Chem. 26, 41-56.

Tessier, D., 1984. Hydratation, gonflement et structuration des matériaux argileux au cours de la dessication et la réhumectation. Doc. Ès Sci. Thesis, Univ. Paris & INRA Versailles, France.

Toth, J.R., 1980. Deposition of submarine crusts rich in manganese and iron. Bull. Geol. Soc. Am. 91, 44-54.

Usui, A., Yuasa, M., Yokota, M., Nishimura, A., Murakami, M.F., 1986. Submarine hydrothermal manganese deposits from the Ogasawara (Bonin) Arc, off the

Japan Islands. Mar. Geol. 73, 311-322.

Usui, A., Bau, M., Yamazaki, T., 1997. Manganese microchimneys buried in the Central Pacific pelagic sediments: evidence of intraplate water circulation. Mar. Geol. 141, 269-285.

Vacquier, V., Sclater, J.G., 1967. Studies in the thermal state of the earth, the 21st paper: heat flow, Eastern Pacific. Bull. of the Earthq. Res. Inst. 45, 375-393.

Verlaan, P.A., Cronan, D.S., Morgan, C.L., 2004. A comparative analysis of compositional variations in and between marine ferromanganese nodules and crusts in the South Pacific and their environmental controls. Prog. in Oceanogr. 63, 125-158.

Von Herzen, R.P., Uyeda, S., 1963. Heat flow throught the Eastern Pacific floor. J. Geophys. Res. 68. 4219-4250.

Wheat, C.G., Feely, R.A., Mottl, M.J., 1996. Phosphate removal by oceanic hydrothermal processes. An update of the phosporus budget in the oceans. Geochim. Cosmochim. Acta 60, 3593-3608.

Captions

Fig. 1: a) General map of the Ticoflux field area with location of the Dorado outcrop and the ODP hole 1039 (modified from Fisher et al., 2003). b) Location of the studied cores on the southwest side of the outcrop.

Fig. 2: Sedimentary sequence of gravity core GC50 and location of the studied samples (depth below sea floor (bsf) are indicated). The relative abundance of various sedimentary components in the core is shown, estimated from smear slides and SEM observations. Continuous line: dominant; dashed line: minor and no line: not detected. 1 = volcanic glass particles and siliceous microfossils; 2 = clay minerals; 3 = phillipsite; 4 = Mn oxides; 5 = Fe oxides; 6 = apatite.

Fig. 3: SEM images of reference sediment and GC50 samples (a) hemipelagic mud from the reference sediment. (b) Mn-Fe oxides encrusting siliceous fossils in sample GC50 at 2 cm bsf. (c) Void filling by authigenic phillipsite in clay-rich sediment at 52 cm bsf. (d) Mn oxides with honeycomb structure in the non-indurated Mn crust at 100 cm bsf. (e) Mn oxides encrusting authigenic phillipsite (100 cm bsf). (f) Authigenic euhedral crystals of apatite at 120 cm bsf. Abbreviations: Cl = detrital smectite; Ap = apatite; F = siliceous microfossils; Ox =oxides; Ph = phillipsite and Vg = volcanic glass.

Fig. 4: XRD patterns of the reference sediment and three GC50 samples showing the mineralogical changes with depth. Peak labels: B = barite, Ap = apatite, H = halite, P = phillipsite, Pl = plagioclase, Q = quartz, SM = smectite, T = todorokite.

Fig. 5: Fitting of the 4-9°2θ XRD reflections band of the air-dried and glycolated preparations for the reference sediment (a) and sample at 52 cm bsf (b).

Fig. 6: TEM images of impregnated samples at 100 cm (a) and 124 cm (b). (a) Mn concretions with concentric zonation, showing 10Å-vernadite (Ve) in the center and todorokite (T) with lath like morphology on the edge. (b) Apatite (Ap) and Fe oxide (G, goethite) with associated SAED (selected area diffraction electron) pattern.

Fig. 7: Al-Fe-Mn ternary diagram for GC50 sediment samples and reference sediments.

Fig. 8: Depth plots of elemental enrichment factors (Ei), on a log-scale, for GC50 samples (except for the surface nodule at 2 cm bsf) relative to average reference sediment. For major elements (a and b) and trace elements (c).

Fig. 9: REE patterns normalized to PAAS (Post-Archean Australian Shale, Mc Lennan, 1989). For comparison, we included patterns for Pacific seawater from 2576 m depth (Alibo and Nozahi, 1999). Seawater values were multiplied by factor 10^6 for comparison.

Fig. 10: Ce/Ce* and Eu/Eu* changes with depth for all GC50 samples. The solid lines = seawater values; dotted lines = average of the reference samples with the standard deviation. Open filled = surface nodule at 2 cm bsf and nonindurated Mn oxide layer at

100 cm bsf.

Fig. 11: Plot of Y vs. P_2O_5 for GC50 and reference samples. The ratio valid for organogenic apatite is shown as a line (Marchig et al, 1999). Filled circles are GC50 samples, and open circles are reference samples.

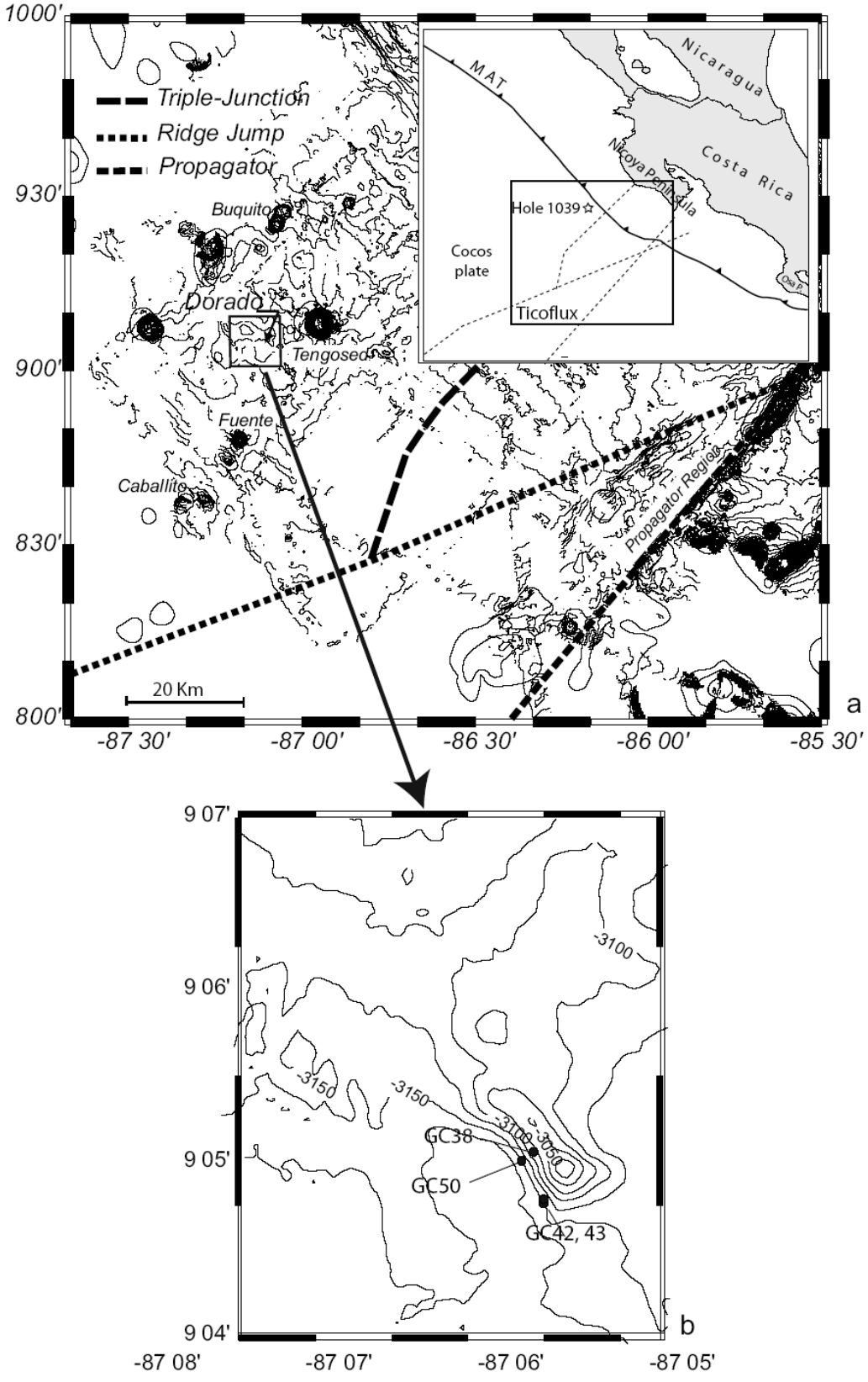
Triple-Junction
Ridge Jump
Propagator
Buquito
Dorado
Tengosed
Fuente
Caballito
Propagator Region
20 Km
1000'
930'
900'
830'
800'
-87 30'
-87 00'
-86 30'
-86 00'
-85 30'
a
MAT
Nicaragua
Costa Rica
Nicoya Peninsula
Hole 1039
Cocos plate
Ticoflux
Osa P.
9 07'
9 06'
9 05'
9 04'
-87 08'
-87 07'
-87 06'
-87 05'
-3100
-3150
-3150
-3100
-3050
GC38
GC50
GC42, 43
b

Fig. 1

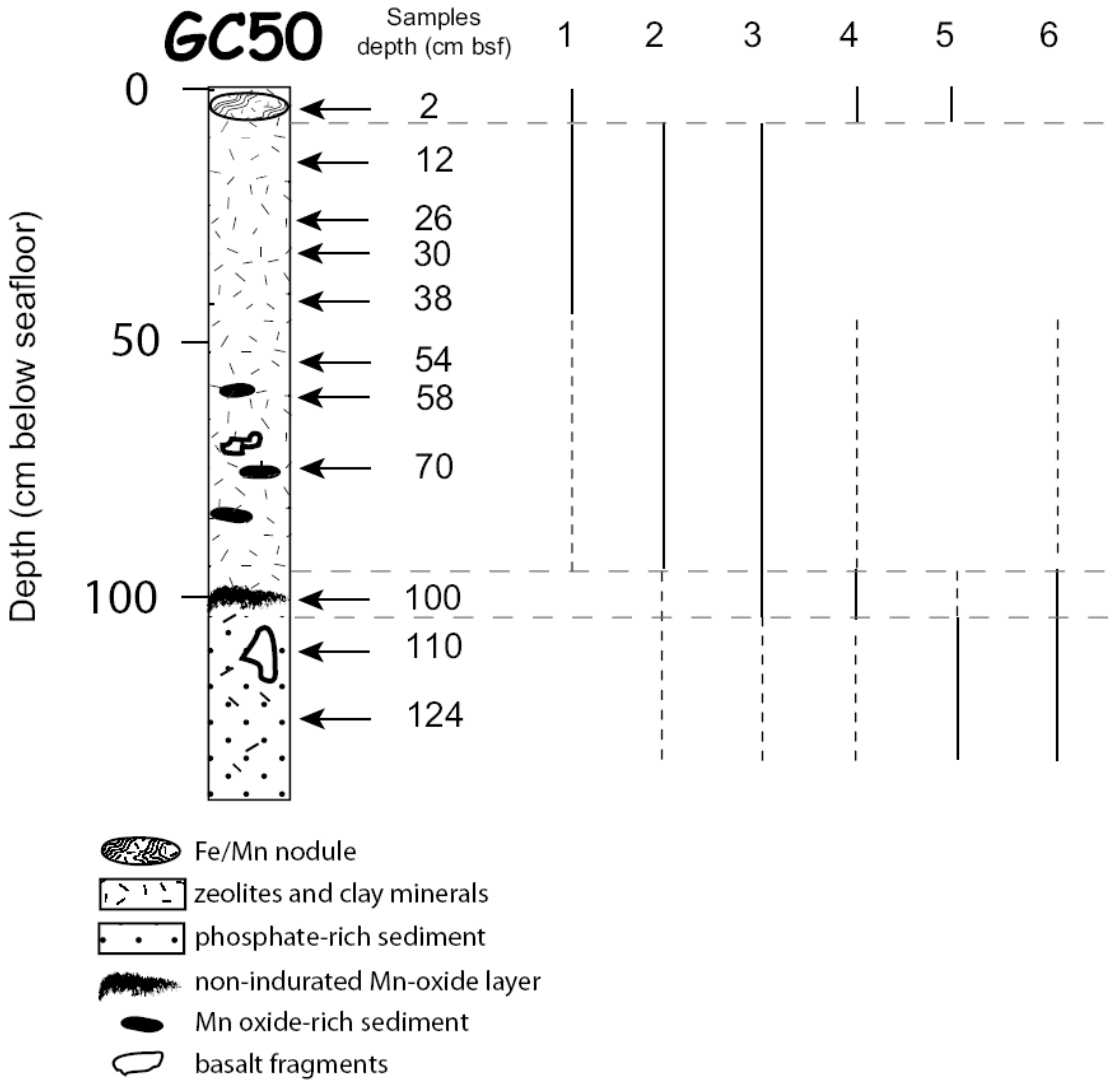
GC50
Samples
depth (cm bsf)
1
2
3
4
5
6
0
50
100
Depth (cm below seafloor)
2
12
26
30
38
54
58
70
100
110
124
Fe/Mn nodule
zeolites and clay minerals
phosphate-rich sediment
non-indurated Mn-oxide layer
Mn oxide-rich sediment
basalt fragments

Fig.2

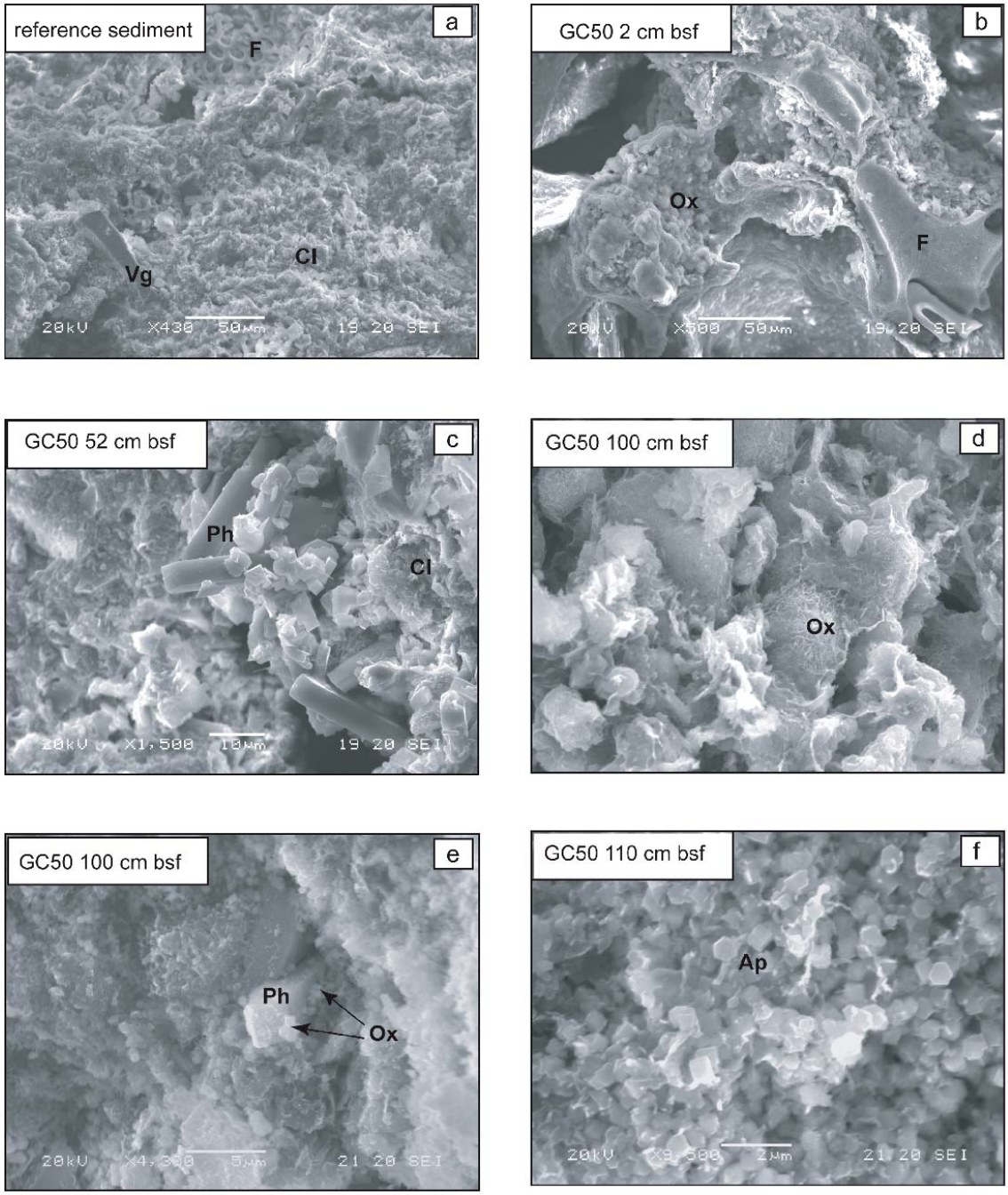
reference sediment
a
F
Vg
Cl
20kV X430 50µm 19 20 SEI
GC50 2 cm bsf
b
Ox
F
20kV X500 50µm 19 20 SEI
GC50 52 cm bsf
c
Ph
Cl
20kV X1,500 10µm 19 20 SEI
GC50 100 cm bsf
d
Ox
GC50 100 cm bsf
e
Ph
Ox
20kV X4,300 5µm 21 20 SEI
GC50 110 cm bsf
f
Ap
20kV X9,500 2µm 21 20 SEI

Fig. 3

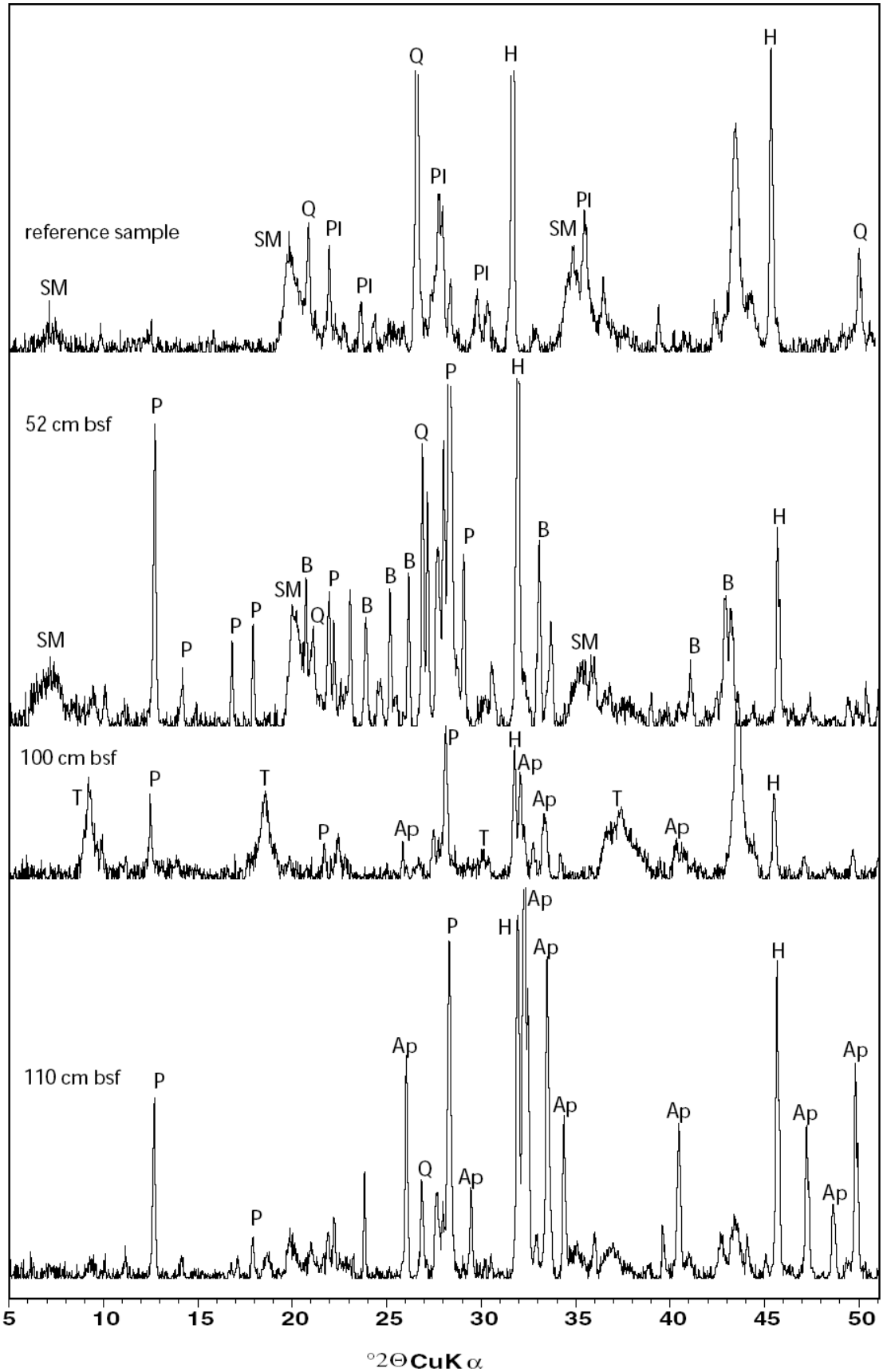
reference sample
52 cm bsf
100 cm bsf
110 cm bsf
SM
Q
PI
H
P
B
T
Ap
5
10
15
20
25
30
35
40
45
50
°2ΘCuKα

Fig. 4

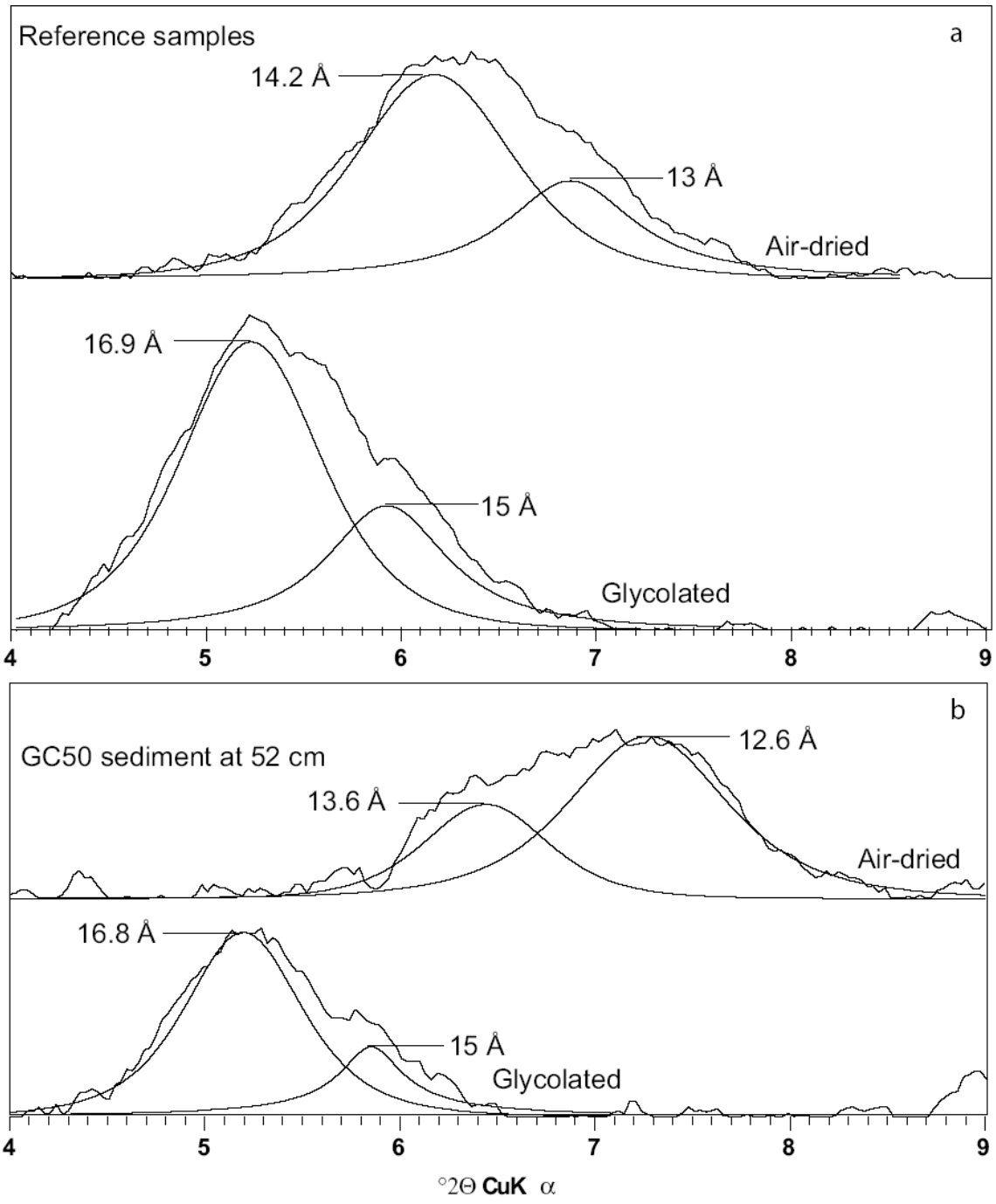
Reference samples
a
14.2 Å
13 Å
Air-dried
16.9 Å
15 Å
Glycolated
4
5
6
7
8
9
b
GC50 sediment at 52 cm
12.6 Å
13.6 Å
Air-dried
16.8 Å
15 Å
Glycolated
4
5
6
7
8
9
°2Θ CuK α

Fig. 5

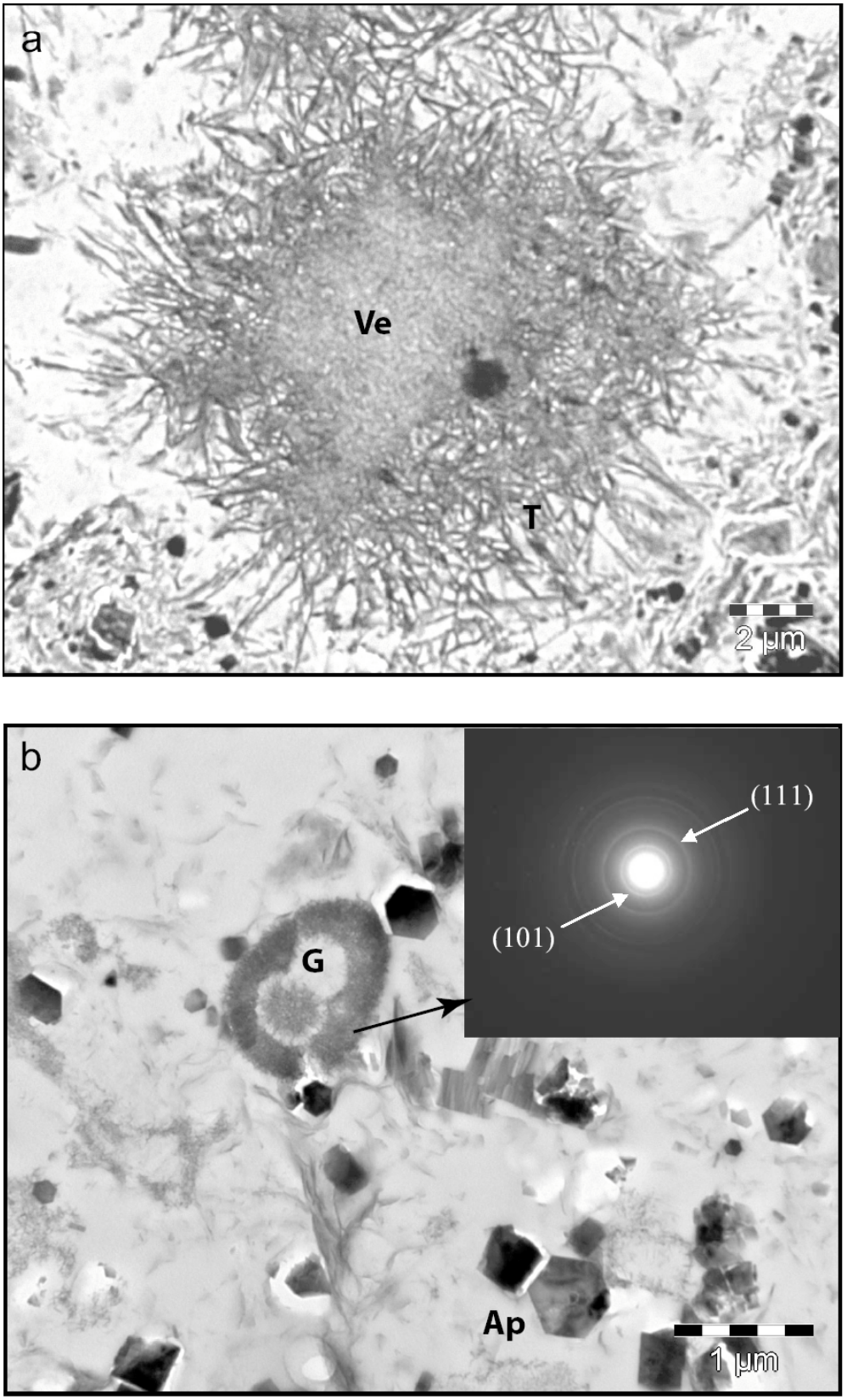

Fig. 6

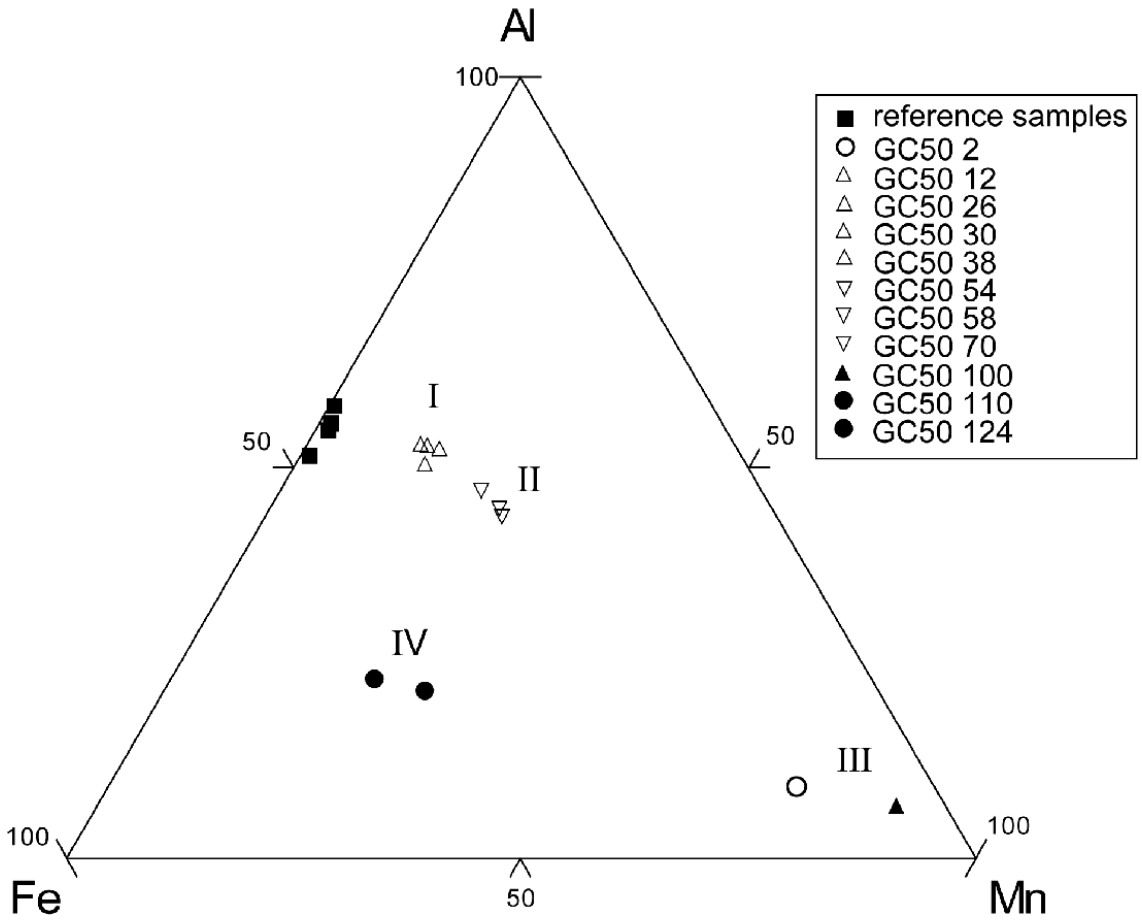
Al
100
50
50
100
100
Fe
50
Mn
I
II
III
IV
reference samples
GC50 2
GC50 12
GC50 26
GC50 30
GC50 38
GC50 54
GC50 58
GC50 70
GC50 100
GC50 110
GC50 124

Fig. 7

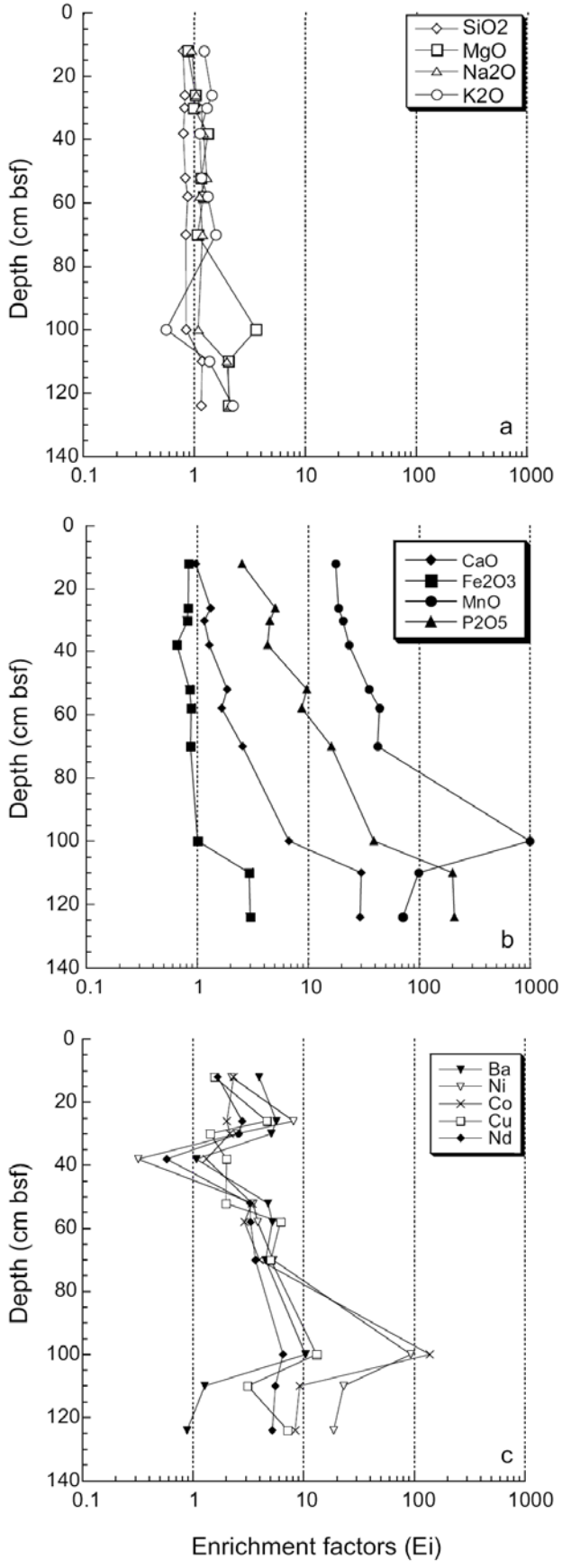
SiO2
MgO
Na2O
K2O
a
CaO
Fe2O3
MnO
P2O5
b
Ba
Ni
Co
Cu
Nd
c
Depth (cm bsf)
Enrichment factors (Ei)
0
20
40
60
80
100
120
140
0.1
1
10
100
1000

Fig. 8

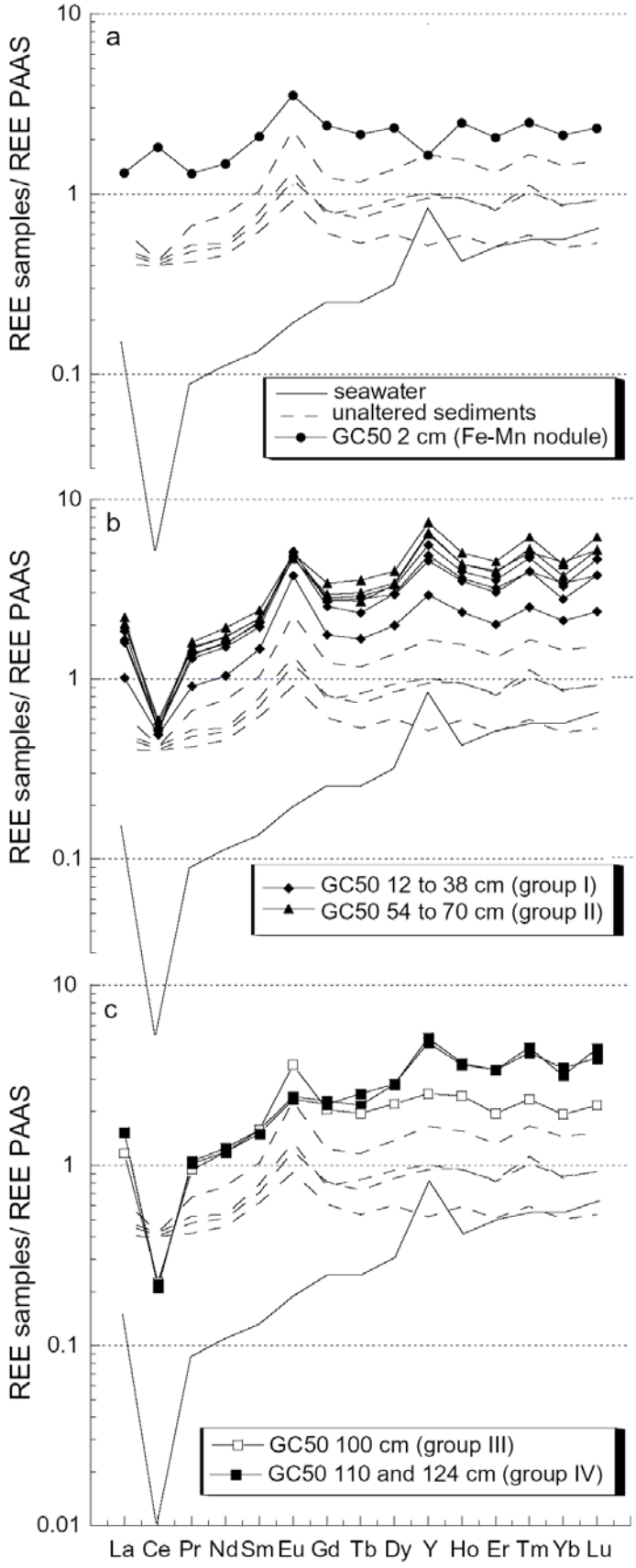
a
b
c
REE samples/ REE PAAS
10
1
0.1
0.01
seawater
unaltered sediments
GC50 2 cm (Fe-Mn nodule)
GC50 12 to 38 cm (group I)
GC50 54 to 70 cm (group II)
GC50 100 cm (group III)
GC50 110 and 124 cm (group IV)
La Ce Pr Nd Sm Eu Gd Tb Dy Y Ho Er Tm Yb Lu

Fig. 9

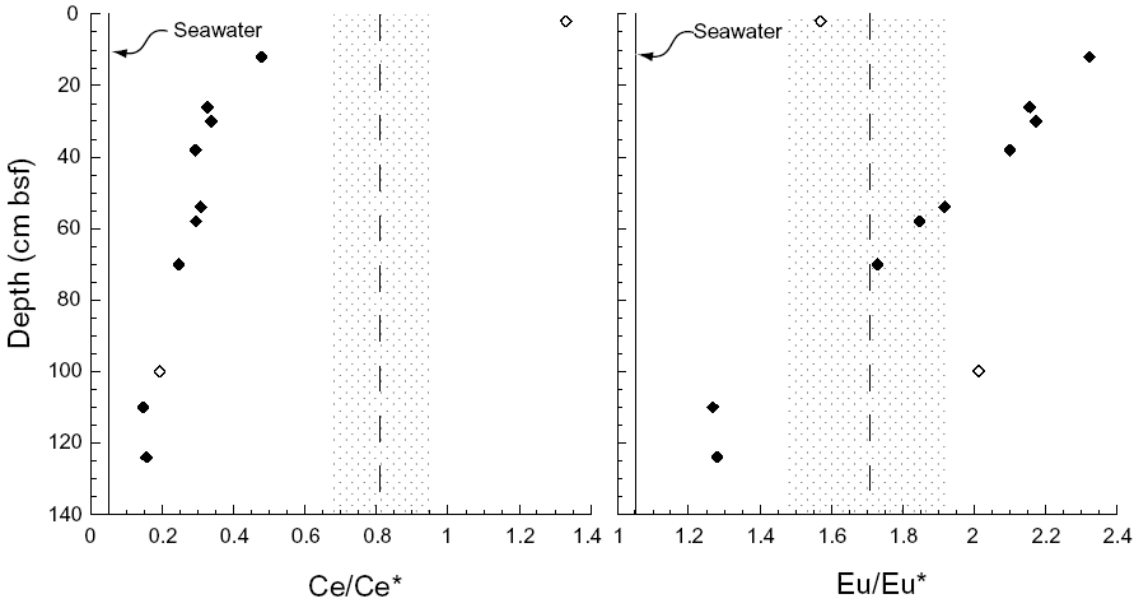
Seawater
Seawater
Depth (cm bsf)
0
20
40
60
80
100
120
140
0
0.2
0.4
0.6
0.8
1
1.2
1.4
1
1.2
1.4
1.6
1.8
2
2.2
2.4
Ce/Ce*
Eu/Eu*

Fig. 10

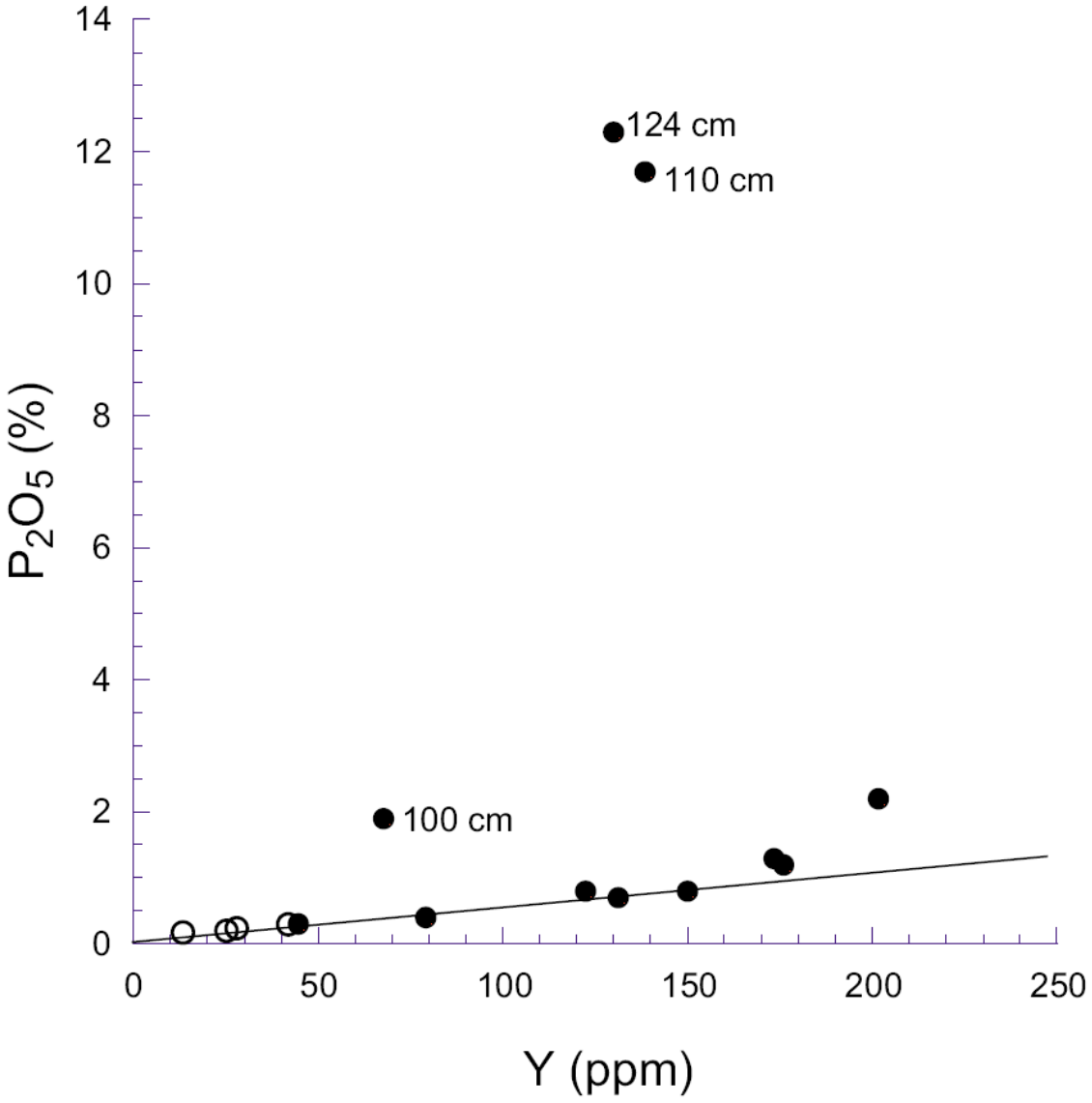

Fig. 11